# Attoclock Photoelectron Interferometry with Two-Color Corotating Circular Fields to Probe the Phase and the Amplitude of Emitting Wave Packets

Meng Han,[1] Peipei Ge,[1] Yun Shao,[1] Qihuang Gong,[1,3] and Yunquan Liu[1,2,3,4,*]
[1]School of Physics and State Key Laboratory for Mesoscopic Physics, Peking University, Beijing 100871, China
[2]Center for Applied Physics and Technology, HEDPS, Peking University, Beijing 100871, China
[3]Collaborative Innovation Center of Quantum Matter, Beijing 100871, China
[4]Collaborative Innovation Center of Extreme Optics, Shanxi University, Taiyuan, Shanxi 030006, China

(Received 24 October 2017; published 15 February 2018)

We employ attosecond angular streaking with photoelectron interferometric metrology to reveal electron sub-Coulomb-barrier dynamics. We use a weak perturbative corotating circularly polarized field (800 nm) to probe the strong-field ionization by an intense circularly polarized field (400 nm). In this double-pointer attoclock photoelectron interferometry, we introduce a spatially rotating temporal Young's two-slit interferometer, in which the oppositely modulated wave packets originating from consecutive laser cycles are dynamically prepared and interfered. Developing a Fourier-transform algorithm on energy-resolved photoelectron interferograms, we can directly extract the amplitude and the phase of emitting electron wave packets from strong-field ionization.

DOI: 10.1103/PhysRevLett.120.073202

Coherent imaging of electron wave packets has attracted wide interest in modern sciences [1]. For strong-field ionization, the amplitude and the phase of the ionized electron wave packet could give direct insights of electron dynamics in the classically forbidden, sub-Coulomb-barrier region. Benefiting from that the laser pulse duration approaches to the natural time scale of intra-atomic electron dynamics, one was allowed to image the amplitude or the phase of an electron wave function on the attosecond scale, such as measuring the angular components of the wave packet with attosecond pulse trains synchronized with an infrared light field [2], probing bound-state wave packets in a pump-probe scheme [3], and extracting the Coulomb scattering phase from photoelectron holography [4].

Alternatively, using a circularly polarized femtosecond laser pulse, dubbed as attosecond angular streaking or attoclock [5–9] (the rotating laser electric vector looks like a pointer), one can transform the rotation of the pointer polarization to the attosecond time resolution. Using the circular polarization, the rescattering of the liberated electron with its parent ion can be avoided and the electron is considered to move classically. Thus, the electron momentum will be approximately shown to point at an angle of 90° relative to the laser electric-field direction at the ionizing instant. In attoclock experiments [5–9], the photoelectron interference effect has been ignored. Indeed, interference structure in photoelectron momentum distribution contains fruitful information. Generally, at a given time $t_0$ in circular polarization, an ionized electron wave packet (EWP) can be described as $\psi_0 = W_0 e^{i\varphi_0}$, where $W_0$ is the amplitude and $\varphi_0$ is the phase. This wave packet will interfere with the subsequent EWP that is emitted after one laser period $T$ at a radial direction of the momentum plane (intercycle interference). The interferogram of the two EWPs is given by $I^{(\mathrm{one})} = |\psi_0 + \psi_0 e^{ib}|^2$ [$b = -\int_{t_0}^{t_0+T} [\boldsymbol{p} + \boldsymbol{A}(t)]^2/2 + I_p dt = -(\boldsymbol{p}^2/2 + U_p + I_p)T$ is the phase difference due to their temporal separation, where $\boldsymbol{p}$ is the canonical momentum, $\boldsymbol{A}(t)$ is the laser vector potential, $I_p$ is the ionization potential, and $U_p$ is the ponderomotive energy]. It appears as above-threshold ionization (ATI) peaks with one photon energy interval [10].

Recently, the two-color counterrotating circular fields have been used to produce high harmonics of circular polarization [11,12], to control above-threshold ionization [13], and to enhance double ionization [14,15]. In those cases, substantial rescattering events will take place. For the two-color corotating circular fields with comparable intensities, the ionization from both fields has the significant contribution to the photoelectron momentum distributions [13], so that it is hard to establish the attoclock to probe the subbarrier dynamics.

In this Letter, employing two-color corotating circular fields, we demonstrate a double-pointer attoclock photoelectron interferometer to probe the phase and the amplitude of emitting wave packets from strong-field ionization. To that end, we manipulate the rotating barrier on both radial and angular directions, by adding a perturbative corotating laser field at the half frequency of the ionizing laser pulse [see Fig. 1(a)]. The synthesized laser field is $\boldsymbol{E}(t) = [E_{400}\cos(\omega t) + E_{800}\cos(0.5\omega t + \varphi_L)]\boldsymbol{z} + [E_{400}\sin(\omega t) + E_{800}\sin(0.5\omega t + \varphi_L)]\boldsymbol{x}$, where $\varphi_L$ is the phase delay between the two pulses. The intense second harmonic field (400 nm) is used to ionize atoms [16]. The fundamental wave (800 nm) is a very weak perturbative probe pulse, and

 

its intensity is controlled to be below 0.5% of the ionizing field.

This is equal to adding an hour pointer (800 nm) into an attoclock that possesses only a single minute pointer (400 nm). The hour pointer will break the symmetry of the original light field, so that both the amplitude and the phase of emitting EWPs are modified accordingly. One can describe the modulated EWP as $\psi_0 e^{-i\varepsilon}$ with a small complex quantity $\varepsilon$, where its real part ($\mathrm{Re}[\varepsilon]$) is the phase variation as $\varphi = \varphi_0 - \mathrm{Re}[\varepsilon]$ and its imaginary part ($\mathrm{Im}[\varepsilon]$) corresponds to the amplitude modification as $W = W_0 e^{\mathrm{Im}[\varepsilon]}$. The imaginary phase $\mathrm{Im}[\varepsilon]$ is related with the ionization probability, which originates from the subbarrier process since the classical propagation outside the barrier approximately does not change its probability amplitude [17]. At ionization instants of the interfered EWPs, i.e., $t_0$ and $t_0 + T_{400}$, the electron feels the opposite force of the hour pointer under the barrier. The two laser-induced EWPs appear opposite modifications as $\psi_0 e^{-i\varepsilon}$ and $\psi_0 e^{i\varepsilon}$ [see Fig. 1(b)], imprinting the subtle subbarrier effects on its amplitude and phase distributions. For different ionization times, the bent potential barrier rotates and the emitting EWPs will be streaked to different radial directions. Therefore, this scheme can be viewed as a spatially rotating temporal Young's two-slit interferometer.

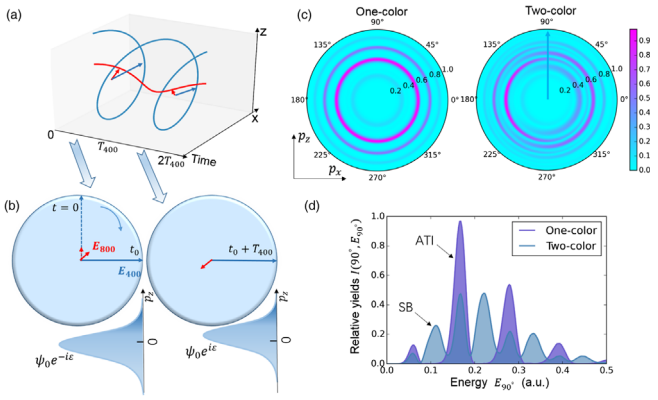


FIG. 1. Principle of double-pointer attoclock photoelectron interferometer. (a) Illustration of corotating two-color [400 nm (ionizing) +800 nm (weak probing)] circularly polarized laser fields at phase delay $\varphi_L = 0$. The arrows indicate their electric-field vectors (like two pointers of a clock) at a pair of ionization instants, $t_0$ and $t_0 + T_{400}$, where $T_{400}$ is a period of the 400 nm field. (b) The track of the clock pointers in the polarization plane and the laser-induced EWPs at $t_0$ and $t_0 + T_{400}$. At time zero the two clock pointers (dashed arrows) are parallel, and then two clock pointers start to rotate with different angular velocities. At the two interfering ionization instants, the directions of the ionizing field (long clock pointer) are the same and those of the short clock pointer are opposite, leading that the potential barrier is modulated inversely. The perturbative clock pointer leaves opposite effects during ionizing, and thus the EWPs record the subbarrier information in their amplitudes and phases, which finally will be mapped into the modification of their interference pattern compared with that in the absence of the probe light. (c) Photoelectron momentum distributions simulated by the SFA model. The final interference fringe between the EWPs illustrated in (b) is marked with the arrow in the direction of polar angle 90°. (d) The photoelectron energy distribution from (c) along the polar angle 90°.

To reveal the effect of the modulation, in Fig. 1(c), we show the photoelectron momentum distributions in one-color and in two-color circular fields at $\varphi_L = 0$, calculated by the strong-field approximation (SFA) model [18]. In the SFA model, after ionization the Coulomb potential is ignored and the mapping relationship between the electron ionization time $t_0$ and emitting angle $\theta$ is strictly established. The transition matrix element is given by $M_{\boldsymbol{p}}^{(\mathrm{SFA})} \sim \int_0^{t_f} d\tau[(\boldsymbol{p} + \boldsymbol{A}(\tau)] \cdot \boldsymbol{E}(\tau))/(\pi\{[\boldsymbol{p} + \boldsymbol{A}(\tau)]^2 + 2I_p\}^3)] \exp\{\int_0^{\tau}(1/2)[\boldsymbol{p} + \boldsymbol{A}(t')]^2 + I_p dt'\}$, where $t_f$ is the pulse turn-off time, and $I_p$ is selected as 0.579 a.u. to match argon atoms. The laser field is synthesized by a six-cycle $\sin^2$-envelope laser pulse at 800 nm, and the peaks of the 800 and 400 nm electric fields are $E_{400} = 0.04$ and $E_{800} = 0.0025$ a.u., respectively.

Within the SFA, an EWP will be streaked to the angle $\theta$ perpendicular to the direction of the ionizing field $E_{400}(t_0)$, which is the ionizing (or "minute") pointer. Thus, the location of the interference fringes among the paired EWPs in Fig. 1(b) can be uniquely determined, which is marked by the blue arrow in Fig. 1(c). In the time domain, a weak probe light will break the homogeny of these EWPs and their interference leads sidebands (SBs) to emerge between the adjacent ATIs, having the angle-dependent feature.

The SBs are involved with the intercycle photoelectron interference of 800 nm field. Thus, the photoelectron momentum distribution in this two-color field [Fig. 1(c), right] can be generally described by the four-EWP interference within two periods of the 800 nm field as $I^{(\mathrm{two})} = |\psi_0 e^{-i\varepsilon} + \psi_0 e^{i\varepsilon+ib} + \psi_0 e^{-i\varepsilon+i2b} + \psi_0 e^{i\varepsilon+i3b}|^2$. The angle- and energy- resolved photoelectron interferogram can be expressed as

$$\begin{aligned} I^{(\mathrm{two})}(\theta, E_\theta) = {} & 2W_0{}^2(e^{-2\mathrm{Im}[\varepsilon]} + e^{2\mathrm{Im}[\varepsilon]}) \\ & + 4W_0{}^2\cos(E_\theta T_{400} + 2\mathrm{Re}[\varepsilon] + a) \\ & + 2W_0{}^2\cos(E_\theta T_{400} - 2\mathrm{Re}[\varepsilon] + a) \\ & + 2W_0{}^2(e^{-2\mathrm{Im}[\varepsilon]} + e^{2\mathrm{Im}[\varepsilon]})\cos(2E_\theta T_{400} + 2a) \\ & + 2W_0{}^2\cos(3E_\theta T_{400} + 2\mathrm{Re}[\varepsilon] + 3a). \end{aligned} \quad (1)$$

Here $a = (U_p + I_p)T_{400}$ is a constant phase. In the frequency domain, the SB emission corresponds to the absorption or emission of a single 800 nm photon from adjacent ATIs, as clearly shown in the electron energy spectrum at an emission angle of 90° [Fig. 1(d)]. In the Supplemental Material [19], we have substituted the experimental measured phase into Eq. (1) and have tested

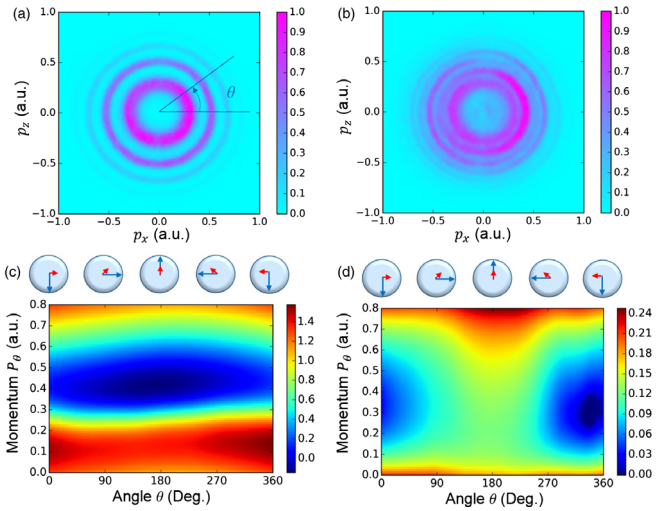


FIG. 2. Measured photoelectron momentum distributions in single (a) and corotating (b) circularly polarized fields at phase delay $\varphi_L = 0$. The extracted real phase $\mathrm{Re}[\varepsilon(\boldsymbol{p}_\theta, \theta)]$ (c) and imaginary phase $\mathrm{Im}[\varepsilon(\boldsymbol{p}_\theta, \theta)]$ (d) from the above measured distributions. The ionization instants are marked on the top of (c) and (d).

the four wave-packet interference geometry by retrieving the photoelectron momentum distribution.

Experimentally, the two-color circularly polarized fields were generated using a Mach-Zehnder interferometer scheme. The fundamental laser pulse (wavelength ~800 nm, pulse duration ~25 fs) was derived from a Ti:sapphire multipass amplifier operating at 3 kHz. The second harmonic was obtained via frequency doubling in a 250-$\mu$m-thick $\beta$-barium borate (BBO) crystal. The relative time delay of the two pulses was controlled by a pair of wedges. The electron momentum distributions of argon atoms were measured by cold-target recoil-ion reaction momentum spectroscopy (COLTRIMS) [20]. The intensity of the 400 nm light was calibrated to be $\sim(1.1 \pm 0.2) \times 10^{14}$ W/cm$^2$ by ATI locations, and that of the 800 nm light was calibrated $\sim(0.44 \pm 0.05) \times 10^{12}$ W/cm$^2$ by comparing electron momentum distributions with the *ab initio* simulations. In the experiment, one needs to realize the perfect circular polarizations for both fields. The experimental setup is presented in the Supplemental Material [19] in detail.

Figures 2(a) and 2(b) show the measured photoelectron momentum distributions in one-color circular field and in two-color circular fields at $\varphi_L = 0$, respectively. After adding the perturbative 800 nm field, both ATIs and SBs show the angle-dependent feature. Note that those two spectra are measured at the same laser pulse at 400 nm. As shown in Fig. 2(b), along the negative $p_x$ axis, the ATI yields are much higher than the SB yields, and the situation is reversed along the positive direction. The calculations by the SFA model agree with the experiments. By comparison with the results in Fig. 1(c), one can see that the angle dependences and variation ranges of ATI and SB peaks are well coincident. We also calculate the photoelectron momentum distributions by the *ab initio* method with numerically solving the time-dependent Schrödinger equation (TDSE) [21]. The calculation by the SFA shows a similar distribution with the result by the TDSE method (see Supplemental Material [19]), suggesting that the SFA is a good approximation for current experimental condition.

To extract the complex phase of wave packets, we transform the electron momentum distribution into angle-resolved energy distribution $I(\theta, E_\theta)$. With this, the equally spaced ATI and SB peaks behave like equally spaced interference fringes [see Supplemental Material [19] for experimental data or Fig. 1(d)], in analogy with traditional optical interferometry [22]. One can see that in this photoelectron interferogram, the amplitude and the phase carried by the EWPs are recorded by the interferometer into a clear modulation of ATI and SB peaks. In traditional optical interferometry, the real-space optical interferogram, $I(x, y)$, can always be described by $I(x, y) = I_0(x, y) + a(x, y) \cos[2\pi f_x x + \varphi(x, y)]$, where $f_x$ is the fringe frequency in the $x$ direction, $\varphi(x, y)$ is the pattern phase contained in the interference term, $I_0(x, y)$ is the interferogram background (also called the zero-frequency component), and $a(x, y)$ describes variations of the fringe visibility. All the components of the interferogram can be extracted through a Fourier-transform approach [22].

In this double-pointer attoclock photoelectron interferometry, the electron streaked angle $\theta$ and the energy $E_\theta$ along the polar angle are in analogy with $y$ and $x$, respectively. As seen from Eq. (1), $2W_0^2 e^{2\mathrm{Im}[\varepsilon]} + 2W_0^2 e^{-2\mathrm{Im}[\varepsilon]}$ (the probability superposition of the two modulated wave packets) corresponds to the background $I_0(x, y)$. The real part of the complex phase corresponds to the pattern phase, i.e., $\varphi(x, y) \sim 2\mathrm{Re}[\varepsilon]$. For the one-color interferogram, $I_0(x, y)$ corresponds to $4W_0^2$ (the probability of two identical unmodulated wave packets) and $\varphi(x, y)$ is a constant number.

The 2D complex phase can be fully extracted using a Fourier-transform algorithm from the electron momentum distributions [Figs. 2(a) and 2(b)]. First, we transform the momentum distributions to angle-resolved energy spectra and do the Fourier transform along each $\theta$. To extract $\mathrm{Im}[\varepsilon]$, we filter out the interference terms from the obtained Fourier spectra, recover the zero-frequency component by the inverse transform, and then utilize the ratio [corresponding to $1/2(e^{2\mathrm{Im}[\varepsilon]} + e^{-2\mathrm{Im}[\varepsilon]})$] between the two-color and one-color results to evaluate $\mathrm{Im}[\varepsilon]$. To extract $\mathrm{Re}[\varepsilon]$, in the two-color Fourier spectrum we shift the frequency component of the interference term [corresponding to $2W_0^2 \cos(3E_\theta T_{400} + 2\mathrm{Re}[\varepsilon] + 3a)$] to the center, and do the inverse transform along each $\theta$. Then we can obtain $2\mathrm{Re}[\varepsilon]$ (it is proportional to the argument of the obtained complex number). The algorithm and the extraction process are presented in the Supplemental Material [19]. Note that the phase reconstruction method is a pure mathematical approach, which is independent with any tunneling or

multiphoton models of strong-field ionization. In the deep tunneling regime, photoelectron holography [23] has been demonstrated. However, it is hard to read the information from the hologram. Here, concentrating on the time-resolved interference patterns, we can extract the amplitude and the phase of the wave packets.

Figures 2(c) and 2(d) show the extracted real phase $\mathrm{Re}[\varepsilon]$ and imaginary phase $\mathrm{Im}[\varepsilon]$ with respect to the emission angle. We illustrate the corresponding ionization instants using a clock on the top of the panels (the angle bin size is 2° and the time resolution ~8 as). From the distributions, one can see that the modulation at the most probable momentum is less for both the real and the imaginary phase, and the two flanks of the EWP are affected mostly when the probing perturbative field is on. When the two pointers of the attoclock are parallel ($\theta = 180°$), the Coulomb barrier is bent further by the short clock pointer to the same direction, and the emitting EWP will become wider and its center location is not changed obviously. Thus, along the direction the real phase has the minima at the central part, and the imaginary phase shows that the high-momentum part of the EWP is most enhanced, indicating the subbarrier process serves as a high-pass filter in momentum space. When the two clock pointers are perpendicular ($\theta = 0°$), the EWP experiences a lateral force under the barrier, and the force will change its peak location and rearrange the phase remarkably. Thus, along the direction the real phase oscillates obviously, and the imaginary phase indicates that the lateral shift of the EWP causes its two flanks slight enhancement.

From the extracted imaginary phase, we are able to image the momentum distribution of EWP when it emerges from atoms. To that end, one needs to subtract the laser-streaking momentum ($E_{400}/\omega \approx 0.351$ a.u.) from the measured momentum. First, we reconstruct the background $4W_0(\theta, P_\theta)^2$ from the one-color interferogram through inversely transforming its zero-frequency component in the Fourier spectrum, then reduce the streaking momentum. Using the relation of the streaking angle $\theta$ to the birth time $t_0$, the momentum distribution of EWP $W_0(t_0, P_{\mathrm{exit}})$ in single circular field (400 nm) at the birth time is obtained, as shown in Fig. 3(a). It is shown that the transversal momentum of EWP is not centered at zero when the EWP is freed, because the electron experiences the rotating force under the barrier, reflecting the nonadiabatic nature of the interaction between laser fields and atoms [24,25]. Combining the extracted time-resolved $\mathrm{Im}[\varepsilon]$ [Fig. 2(d)] with the extracted $W_0(t_0, P_{\mathrm{exit}})$, in Fig. 3(b) we reconstruct the evolution of the modulated EWP using $W(t_0, P_{\mathrm{exit}}) = W_0(t_0, P_{\mathrm{exit}})e^{\mathrm{Im}[\varepsilon]}$. From $t_0 = 0$ to $t_0 = T_{400}/2$, the two clock pointers are rotating from parallel to vertical and the probability of EWP decreases nonlinearly. The ionized flux is highly dependent on the electric-field component along the long clock-pointer direction. The emitting wave packet is dynamically imaged within the resolution of a few attoseconds. Theoretical work [24,26] has pointed out the initial momentum will shift in a circular field and recent experiments [9,27] verified the prediction.

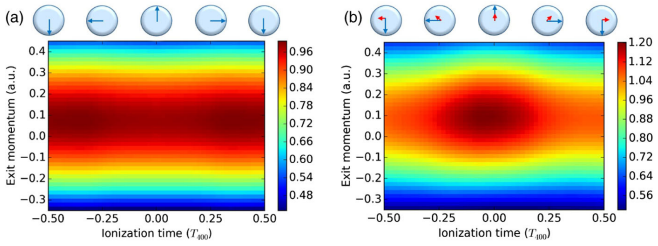


FIG. 3. Dynamic imaging of emitting EWPs. Reconstructed attosecond-resolved emitting EWPs in momentum space in one-pointer attoclock (a) and double-pointer attoclock (b).

It is worth mentioning that there is another working mode of the double-pointer attoclock photoelectron interferometer. If one focuses on a certain radial direction of photoelectron momentum distribution ($P_\theta$) at a given $\theta$, and then scans the laser phase delay $\varphi_L$ to measure the interferogram variation along the direction, it is equal to fixing the long clock-pointer direction and rotating the short clock pointer, rather than the two pointers simultaneously rotating in Fig. 2. Figures 4(a) and 4(b) depict the measured momentum distribution at two

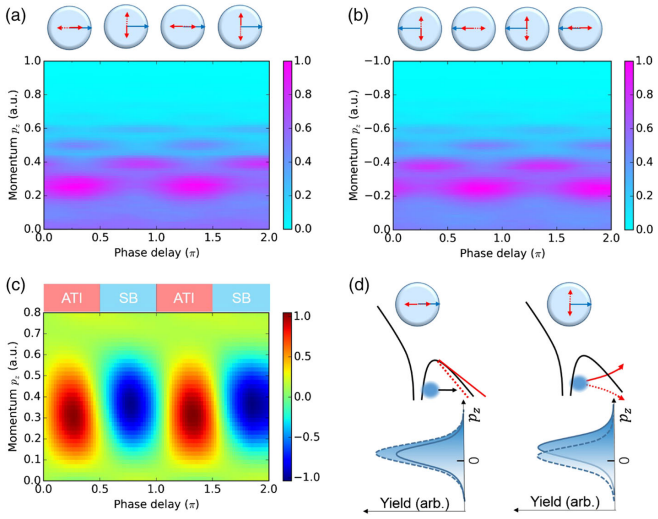


FIG. 4. Scanning the short clock-pointer working mode of the double-pointer attoclock photoelectron interferometer. Measured electron momentum distribution along the positive $p_z$ axis (a) and along the negative $p_z$ axis (b) with respect to the phase delay between the two colors. $p_x$ and $p_y$ are both confined within a small bin [−0.02, 0.02]. The interferogram at each phase delay is contributed to by two orientations of the short pointer, corresponding to the birth times of the two interfered EWPs. (c) Differential distribution between the extracted backgrounds from (a) and (b). The differential value is normalized to [−1, 1], from the SB (blue area) to the ATI (red area) dominant region. (d) The deformed Coulomb potentials and the initial momentum distributions of the EWPs when two clock pointers are parallel and perpendicular, respectively. Because the long clock pointer is along the $x$ axis, the EWP approximately shows a Gaussian along $p_z$ at the exit.

radial directions (along positive $p_z$ and along negative $p_z$) with respect to the phase delay in one cycle of the 800 nm field. The ATI and SB peaks oscillate alternately with the time delay of roughly $T_{400}/2$ and the polarizations of the two clock pointers are shown at the top of the figures. We retrieved the background term $2W_0^2 e^{2\mathrm{Im}[\varepsilon]} + 2W_0^2 e^{-2\mathrm{Im}[\varepsilon]}$ for the above two distributions through the extraction algorithm. The difference between the backgrounds is shown in Fig. 4(c). In the result, it is clear that the ATI peaks are dominant when the two clock pointers are parallel and the SBs are dominant when they are perpendicular.

In Fig. 4(d), we give an interpretation on the formation of ATIs and SBs. For the two-pointer parallel case, the potential barrier is lifted or lowered by the weak clock pointer, and the emitting EWPs are not segregated in the momentum space, so the ATI peaks are dominant. Whereas for the orthogonal case, the lateral force will shift the EWPs into reverse directions, so that the EWPs are not well overlapped and the ATIs will be weak. The phase variation of the EWP causes the interference fringes to shift significantly, and thus the SB peaks are dominant.

In conclusion, we introduce a novel double-pointer attoclock photoelectron interferometer to probe the electron subbarrier dynamics. This photoelectron interferometry largely extends the capacity of attosecond angular streaking, equipped with the ability of photoelectron interferometric metrology. The measured photoelectron angular distributions are in perfect circular polarization, allowing us to extract the phase and the amplitude of the emitting wave packets. The initial momentum distribution of emitting electron wave packets can be well characterized by this approach. This study provides direct insights into the basic properties of laser-induced ionization, following the evolution of the atomic electronic wave function within the temporal resolution of several attoseconds. The double-pointer attoclock photoelectron interfereometer could be used to further explore the oriented molecules to image molecular electronic wave functions and to probe the dynamics of spin-polarized electrons [28,29].

This work is supported by the National Science Foundation of China (Grants No. 11434002, No. 11774013, and No. 11527901).

*Yunquan.liu@pku.edu.cn

[1] M. J. J. Vrakking, Phys. Chem. Chem. Phys. **16**, 2775 (2014).
[2] D. M. Villeneuve, P. Hockett, M. J. J. Vrakking, and H. Niikura, Science **356**, 1150 (2017).
[3] J. Mauritsson *et al.*, Phys. Rev. Lett. **105**, 053001 (2010).
[4] Y. Zhou, O. I. Tolstikhin, and T. Morishita, Phys. Rev. Lett. **116**, 173001 (2016).
[5] P. Eckle, A. N. Pfeiffer, C. Cirelli, A. Staudte, R. Dörner, H. G. Muller, M. Büttiker, and U. Keller, Science **322**, 1525 (2008).
[6] P. Eckle, M. Smolarski, P. Schlup, J. Biegert, A. Staudte, M. Schöffler, H. G. Muller, R. Dörner, and U. Keller, Nat. Phys. **4**, 565 (2008).
[7] L. Torlina *et al.*, Nat. Phys. **11**, 503 (2015).
[8] M. Li, Y. Liu, H. Liu, Q. Ning, L. Fu, J. Liu, Y. Deng, C. Wu, L. Y. Peng, and Q. Gong, Phys. Rev. Lett. **111**, 023006 (2013).
[9] M. Li, M.-M. Liu, J.-W. Geng, M. Han, X. Sun, Y. Shao, Y. Deng, C. Wu, L.-Y. Peng, Q. Gong, and Y. Liu, Phys. Rev. A **95**, 053425 (2017).
[10] P. Agostini, F. Fabre, G. Mainfray, G. Petite, and N. K. Rahman, Phys. Rev. Lett. **42**, 1127 (1979).
[11] O. Kfir *et al.*, Nat. Photonics **9**, 99 (2015).
[12] A. Fleischer, O. Kfir, T. Diskin, P. Sidorenko, and O. Cohen, Nat. Photonics **8**, 543 (2014).
[13] C. A. Mancuso *et al.*, Phys. Rev. A **91**, 031402 (2015).
[14] S. Eckart *et al.*, Phys. Rev. Lett. **117**, 133202 (2016).
[15] C. A. Mancuso *et al.*, Phys. Rev. Lett. **117**, 133201 (2016).
[16] X. Xie, T. Wang, S. Yu, X. Lai, S. Roither, D. Kartashov, A. Baltuška, X. Liu, A. Staudte, and M. Kitzler, Phys. Rev. Lett. **119**, 243201 (2017).
[17] O. Pedatzur *et al.*, Nat. Phys. **11**, 815 (2015).
[18] D. B. Milošević, G. G. Paulus, D. Bauer, and W. Becker, J. Phys. B **39**, R203 (2006).
[19] See Supplemental Material at http://link.aps.org/supplemental/10.1103/PhysRevLett.120.073202 for the experimental setup, extraction algorithm of complex phase, retrieving electron momentum distribution, *ab initio* Method and results.
[20] J. Ullrich, R. Moshammer, A. Dorn, R. Dörner, L. Ph. H. Schmidt, and H. Schmidtböcking, Rep. Prog. Phys. **66**, 1463 (2003).
[21] V. Mosert and D. Bauer, Comput. Phys. Commun. **207**, 452 (2016).
[22] M. Takeda, H. Ina, and S. Kobayashi, J. Opt. Soc. Am. **72**, 156 (1982).
[23] Y. Huismans *et al.*, Science **331**, 61 (2011).
[24] M. Han, M. Li, M.-M. Liu, and Y. Liu, Phys. Rev. A **95**, 023406 (2017).
[25] M. Han, P. Ge, Y. Shao, M.-M. Liu, Y. Deng, C. Wu, Q. Gong, and Y. Liu, Phys. Rev. Lett. **119**, 073201 (2017).
[26] I. Barth and O. Smirnova, Phys. Rev. A **84**, 063415 (2011).
[27] M.-M. Liu, M. Li, Y. Shao, M. Han, Q. Gong, and Y. Liu, Phys. Rev. A **96**, 043410 (2017).
[28] D. Trabert, A. Hartung, S. Eckart, F. Trinter, A. Kalinin, M. Schöffler, L. Ph. H. Schmidt, T. Jahnke, M. Kunitski, and R. Dörner, Phys. Rev. Lett. **120**, 043202 (2018).
[29] M.-M. Liu, Y. Shao, M. Han, P. Ge, Y. Deng, C. Wu, Q. Gong, and Y. Liu, Phys. Rev. Lett. **120**, 043201 (2018).